Math Geosci (2014) 46:625–645
DOI 10.1007/s11004-013-9484-z

SPECIAL ISSUE

Conditioning of Multiple-Point Statistics Facies Simulations to Tomographic Images

Tobias Lochbühler · Guillaume Pirot · Julien Straubhaar · Niklas Linde

Received: 17 December 2012 / Accepted: 28 July 2013 / Published online: 7 September 2013

Abstract Geophysical tomography captures the spatial distribution of the underlying geophysical property at a relatively high resolution, but the tomographic images tend to be blurred representations of reality and generally fail to reproduce sharp interfaces. Such models may cause significant bias when taken as a basis for predictive flow and transport modeling and are unsuitable for uncertainty assessment. We present a methodology in which tomograms are used to condition multiple-point statistics (MPS) simulations. A large set of geologically reasonable facies realizations and their corresponding synthetically calculated cross-hole radar tomograms are used as a training image. The training image is scanned with a direct sampling algorithm for patterns in the conditioning tomogram, while accounting for the spatially varying resolution of the tomograms. In a post-processing step, only those conditional simulations that predicted the radar traveltimes within the expected data error levels are accepted. The methodology is demonstrated on a two-facies example featuring channels and an aquifer analog of alluvial sedimentary structures with five facies. For both cases, MPS simulations exhibit the sharp interfaces and the geological patterns found in the training image. Compared to unconditioned MPS simulations, the uncertainty in transport predictions is markedly decreased for simulations conditioned to tomograms. As an improvement to other approaches relying on classical smoothness-constrained geophysical tomography, the proposed method allows for: (1) reproduction of sharp interfaces, (2) incorporation of realistic geological constraints and (3) generation of multiple realizations that enables uncertainty assessment.

T. Lochbühler (✉) · N. Linde
Applied and Environmental Geophysics Group, Faculty of Geosciences and Environment, University of Lausanne, Lausanne, Switzerland
e-mail: tobias.lochbuehler@unil.ch

G. Pirot · J. Straubhaar
Center for Hydrogeology and Geothermics, University of Neuchâtel, Neuchâtel, Switzerland

Keywords Multiple-point statistics · Multiple-point direct sampling · Geophysical tomography · Conditioning

1 Introduction

Predictive modeling of subsurface flow and solute transport requires detailed models of the spatial distribution of hydraulic properties. A lot of recent research has focused on finding ways to use geophysical data for hydrological parameter estimation (e.g., Hubbard and Rubin 2000; Linde et al. 2006; Eppstein and Dougherty 1998; Dafflon and Barrash 2012). The benefit of geophysical techniques is that a high number of sensors can be used at rather low costs and with little invasive impact. Data sets of thousands of data points of high spatial density are easily acquired and when these data are inverted, tomographic images of high resolution can be obtained. Unfortunately, inference of the geophysical property distribution from measured data, that is, the process of inversion or tomography, is generally non-unique due to limited data coverage, noisy data and non-linear physics. To overcome this non-uniqueness, the inverse problem is regularized where the most common approach is to explicitly search least-structure models by applying a smoothness constraint. Smoothness-constrained inversions are optimal in the sense of reducing regularization bias (Ory and Pratt 1995) and turned out to be a forceful tool to prevent inversion artifacts. Their main disadvantage is that they produce tomograms that tend to image the subsurface property distributions as blurred or patchy structures and usually fail to recover sharp interfaces or small-scale structures. For accurate flow and transport modeling, we often need models that capture such features since they may control the subsurface connectivity.

The classical geostatistical approach aims at defining a model such that the two-point statistical relations observed in the field are matched (Kitanidis 1997). These methods are invariant towards connectivity patterns (e.g., Gómez-Hernández and Wen 1998; Krishnan and Journel 2003), which means that parameter fields of very different connectivity characteristics can be identical in terms of their probability density function (pdf) or variogram. For example, Zinn and Harvey (2003) showed for parameter fields of near-identical lognormal univariate conductivity distributions, how flow and transport behavior changed dramatically for different connectivity patterns. Various methods have been proposed to fully characterize parameter fields by including the connectivity patterns. Journel and Posa (1990) proposed to describe connectivity by indicator variograms that provide the probability that two distant points share the same indicator value. This approach has further been advanced by modified connectivity functions that account for points within a certain value range that are connected by an arbitrary continuous path (Western et al. 2001). A recent development are multiple-point statistics (MPS) algorithms that simulate parameter fields by accounting for the statistical relations between large sets of points, thereby allowing the reproduction of complex geological structures and connectivity patterns. The algorithms take the statistics from training images that feature the representative patterns that are subject to simulation. MPS approaches make use of the fact that certain geological settings are often built up by a limited number of repeating structural elements.

At the same time, the need to recover geological patterns and facies structures has been recognized and caught up by the geophysics community. The application of pattern-based approaches for the characterization of subsurface structures is a subject of intense research, mainly led by the petroleum industry (e.g., Coléou et al. 2003; de Matos et al. 2007). Caers and Ma (2002) extracted probabilistic facies distributions from seismic data using neural networks on colocated windows of seismic information. Similarly, Moysey et al. (2003) trained neural networks on geological analogs or well data to retrieve facies information from surface ground-penetrating radar (GPR) images. Based on this, Moysey et al. (2006) compared different transform techniques to translate the radargram into a facies classification. They found that textual measures that preserve the spatial structure of the GPR image often outperform measures based on univariate statistics (variance). A rather novel approach was presented by Cardiff and Kitanidis (2009), who developed an inversion scheme in which facies boundaries as well as parameter values within facies are updated by a Bayesian level set methodology. An example of how a GPR cross-section is used to establish a facies model, which in turn is used for flow and transport simulations is given in Rauber et al. (1998). Dafflon and Barrash (2012) use radar tomograms together with neutron borehole logs to condition stochastic simulations of the 3D porosity distribution in a well field. They show that conditioning to tomograms improves both simulated-annealing-based and Bayesian sequential simulation results.

In this study, we present a novel approach of combining geophysical models and conceptual geological knowledge to produce realistic high-definition subsurface facies models. A categorical training image (TI) containing the geological facies information available about the site of interest is converted into a tomogram by geophysical forward and inverse modeling. The tomogram can be seen as a filtered version of the facies TI that is dependent on the spatial distribution of the underlying geophysical property. Information about resolution of the tomographic setup, and about regularization and data error effects are included in the tomogram since all these factors change the 'tomographic filter' and consequently influence the tomography results. The discrete facies TI and its continuous tomogram are combined to form a bivariate TI. A conditioning tomogram is obtained by applying the same tomography procedure to geophysical data that are measured in the field. We then generate MPS simulations by scanning the bivariate TI for patterns found in the conditioning tomogram, in this case, we use tomograms from cross-hole GPR experiments. Compared to conditioning to individual data points placed somewhere in the model domain (e.g., Zhou et al. 2012), we exploit the spatial information in the tomograms which is distributed over the entire domain.

The proposed method circumvents a problem generally inherent in the interpretation of geophysical models: Inferring the true geology from tomographic images requires correcting the models for all inversion effects, that is, one needs to deconvolve the tomogram and the 'tomographic filter' (Singha et al. 2007). Approaches to tackle this problem are linearized resolution analysis (Menke 1989; Day-Lewis et al. 2005) or the use of numerical analogs to field studies (Moysey et al. 2005; Singha and Moysey 2006). Since we are mimicking the geophysical tomography applied to the measured data when creating the bivariate TI, the 'tomographic filter' is implicitly taken into account. This and the fact that conceptual geological information is incorporated at an early stage of the inverse modeling process reduces the risk

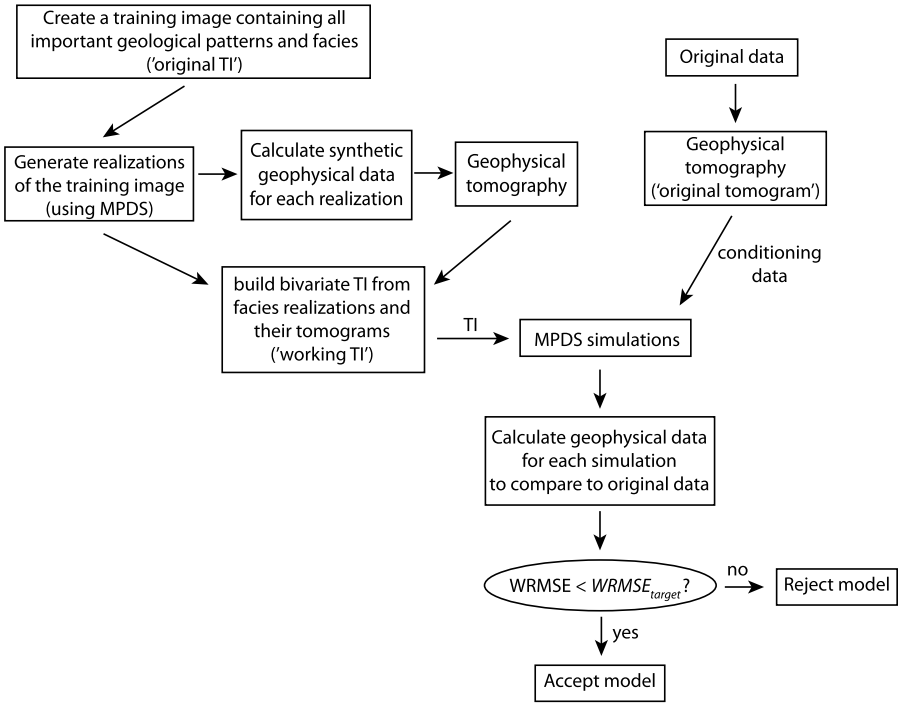

Fig. 1 Schematic workflow of the proposed conditioning method

of misinterpretation due to limited knowledge about the 'tomographic filter' (e.g., Richardson et al. 1987; Rankey and Mitchell 2003). Compared to classical inversion studies, we do not leave the interpreter with a geophysical image on which to base a geological interpretation, but we present a tool to condition a conceptual geological model to the distribution of the inferred geophysical parameters.

2 Methodology

2.1 General workflow

We developed a procedure to condition multiple-point geostatistical simulations to tomographic images. The method builds on the work of Mariethoz et al. (2010b), who present a direct sampling algorithm for multiple-point geostatistical simulations. This multiple-point direct sampling (MPDS) algorithm allows to co-sample from a TI that contains both a distribution of a categorical and a continuous variable. Here, we use a categorical TI featuring characteristic geological structures and its corresponding geophysical tomogram. We then use a tomogram obtained at the field site of interest as a known continuous image to condition the simulation. In this way, we produce a categorical simulation that contains the structures from the categorical training image and whose tomographic image is in agreement with the geophysical tomogram given as input variable. The general workflow is (see also Fig. 1):

1. Invert the available geophysical field data by smoothness-constrained deterministic least-squares inversion. The resulting image is referred to as 'original tomogram' in the following.
2. Choose or create a training image that represents conceptually the expected geological structures/patterns. This is referred to as 'original TI'. This is a crucial step, a poorly chosen training image will severely bias the modeling outcome.
3. Create an ensemble of realizations of the chosen original TI. Here, this is done using MPDS.
4. For each realization of the original TI, generate a synthetic tomogram:
   (a) Assign realistic values of the underlying geophysical parameters (e.g., seismic or radar slowness, electrical resistivity) to the different facies in the realizations. This step can be based on established petrophysical models, for example the CRIM model (complex resistive index method, Tinga et al. 1973; Alharthi and Lange 1987; Roth et al. 1990) or petrophysical relationships inferred from previous investigations (e.g., Hubbard et al. 2001).
   (b) Calculate synthetic geophysical data by simulating field experiments. Model the experiments using a setup similar to that used to acquire the actual data (Moysey et al. 2005). Contaminate the synthetic data with an expected amount of noise.
   (c) Invert the synthetic data. Apply the same modeling parameters (grid discretization, initial model, regularization type and weights) as used to produce the original tomogram (Moysey et al. 2005).
5. Combine the realizations of the categorical original TI and their continuous tomograms to one bivariate 'working TI' that contains the facies and the geophysical parameters as two separate variables.
6. Simulate facies models based on direct sampling:
   (a) Pick a location in the simulation grid whose facies is not yet defined. Retrieve the data events (i.e., certain patterns formed by a pre-defined number of grid cells) centered at this location in the original tomogram and for the facies variable. Then, scan through the ensemble of synthetic tomograms and their corresponding facies models until similar data events are found. 'Similar' here means that the distances between the actual events and the found ones are below some pre-defined threshold. Building the working TI as stacks of two-dimensional models (as will be described in detail later) allows for choosing a scanning procedure so that the spatially varying resolution within a tomogram is accounted for.
   (b) Paste the facies value (at the central node of the data event) found in the TI to the selected location in the simulation grid.
   (c) Randomly pick a new location in the simulation grid and repeat until it is entirely filled.
7. For each simulated facies model, calculate geophysical forward data and compare to the true data. Accept the simulation as a possible model, if the weighted root-mean square error (WRMSE) of the predicted data is below a threshold $\mathrm{WRMSE}_{\mathrm{target}}$.

The resulting ensemble of accepted models forms a possible basis for geological interpretation, flow and transport modeling or uncertainty assessment.

2.2 Deterministic Inversion

Both the original data (i.e., the 'true data' measured in the field) and the predicted data for all facies realizations undergo smoothness-constrained deterministic inversion (steps 1 and 4c in previous section). This inversion type is commonly referred to as Occam's inversion (Constable et al. 1987). In the smoothness-constrained inversion scheme, a model $\mathbf{m}$ is sought that features the least structure possible and still predicts the data within the assumed data error levels. In a general sense, we seek to minimize an objective function $\boldsymbol{\phi}$ that contains both a measure of the data misfit and the model roughness (e.g., Menke 1989):

$$\boldsymbol{\phi} = \left\| \mathbf{C}_d^{-0.5}\left(\mathbf{d} - \mathbf{F}(\mathbf{m})\right)\right\|_2^2 + \alpha \left\| \mathbf{C}_m^{-0.5}(\mathbf{m} - \mathbf{m}_{\text{ref}})\right\|_2^2, \tag{1}$$

where the first term is the error-weighted misfit between original data ($\mathbf{d}$) and data predicted by the forward model ($\mathbf{F}(\mathbf{m})$) in a least-squares sense. The second term is the model misfit or regularization. In Eq. (1),

$\mathbf{C}_d$ is the data error covariance matrix;
$\mathbf{C}_m$ is the model covariance matrix;
α is a trade-off parameter that weights the model regularization with respect to the data misfit term;
$\mathbf{m}_{\text{ref}}$ is a (uniform) reference model.

In our smoothness-constrained inversion, $\mathbf{C}_m$ is an anisotropic first-order differences operator, used to penalize abrupt changes between adjacent model parameters. In this study, horizontal-to-vertical anisotropy ratios of 3:1 and 10:1 were used for the first and the second application. Since the forward problem is non-linear, it is linearized about a reference model (for the first iteration) or the model of the previous iteration (for subsequent iterations), resulting in the following system of equations that is solved with a conjugate gradient solver (Paige and Saunders 1982):

$$\begin{pmatrix} \mathbf{C}_d^{-0.5}\mathbf{J}_k \\ \alpha \mathbf{C}_m^{-0.5} \end{pmatrix} \left(\Delta \mathbf{m}_{k+1} \right) = \begin{pmatrix} \mathbf{C}_d^{-0.5}[\mathbf{d} - \mathbf{F}(\mathbf{m}_k) + \mathbf{J}_k \Delta \mathbf{m}_k] \\ 0 \end{pmatrix}, \tag{2}$$

where k indicates the iteration index and $\mathbf{J}$ is the Jacobian matrix containing the elements $J_{ij} = \partial d_i / \partial m_j$. The model update we solve for, $\Delta \mathbf{m}_{k+1}$, is then used to construct a new model $\mathbf{m}_{k+1} = \mathbf{m}_{\text{ref}} + \Delta \mathbf{m}_{k+1}$. During the inversion, we decrease α consecutively from one iteration to the other in order to start with a smooth model where structure is gradually added to decrease the data misfit. The inversion is stopped when the weighted root-mean squared error $\text{WRMSE}_{\text{target}}$ is reached. The weighting by the data errors implies that for $\text{WRMSE} = 1$, on average all data are fit to their error levels. For a more rigorous description of the inversion scheme, we refer to Linde et al. (2006).

2.3 Multiple-Point Statistics Simulation

Multiple-point statistical simulations describe the procedure to draw fields of facies or geological properties based on the spatial dependencies between a set of points larger than 2. Unlike simulations based on two-point statistics, such as Gaussian sequential simulation, it is insufficient to know only the pdf. Rather, patterns (so-called data

events) of a certain pre-defined size and density are extracted from a training image and the pixel of interest is simulated according to its statistics with respect to previously assigned pixels in the surrounding. The main advantage of MPS over two-point statistics is the ability to deal with non-stationarity and sharp interfaces and consequently allowing simulation of categorical facies models with curvilinear features, which can be crucial to adequately represent connectivity (e.g., Hu and Chugunova 2008).

Classical MPS simulation codes (e.g., Strebelle 2002) scan the training image for patterns and store the multi-point statistics of these in a structured tree. To overcome the limitations due to the large storage demand required by the trees, a list approach was developed by Straubhaar et al. (2011, 2013). In these classical implementations of MPS, the multiple grid approach is used to capture patterns of different scales within the TI (Tran 1994). In this work, we use the MPDS algorithm *DeeSse*, which is an enhanced and commercialized version of the algorithm described by Mariethoz et al. (2010b). Note that in the following, we use 'MPDS' to describe the general direct sampling procedure developed by Mariethoz et al. (2010b), and '*DeeSse*' when we talk about the particular algorithm we used. In *DeeSse* (as in all direct sampling algorithms), the training image is scanned for data events in the simulation grid and directly simulates the pixel of interest, thus avoiding storage limitations, computation of pdf and the use of multiple grids. We give a brief summary of this sampling procedure here; for a complete description we refer to Mariethoz et al. (2010b). If a simulation grid with nodes $\mathbf{x}$ is to be filled using the training image with nodes denoted $\mathbf{y}$, all locations $\mathbf{x}$ are visited successively. At each location $\mathbf{x}$, the n closest neighboring nodes that already have been assigned a value are found and the pattern of their locations and values defines one data event. Starting from a random location in the training image, the training image is systematically scanned for the particular data event. At every location $\mathbf{y}$, the distance between the data event and the event found in the TI is calculated. The data event found in the TI is kept and the node $\mathbf{x}$ of interest is simulated by copying the value from $\mathbf{y}$, if the calculated distance is below a threshold t. If a certain fraction f of the TI has been scanned without success, the event with the smallest distance is accepted and used for simulation. Choosing an appropriate distance measure is crucial for the simulation (e.g., Zhou et al. 2012). We applied an ℓ_1-norm for continuous variables and the sum of non-matching nodes for categorical variables. In addition, *DeeSse* allows to decrease the node density in the group of neighboring nodes to also consider nodes in the pattern recognition that are not directly clustered around the node of interest.

The resolution of a geophysical tomogram is not evenly distributed, but often varies markedly in space. This is due to (1) limitations in signal coverage, and (2) the fact that in non-linear problems, the resolution depends on the property distribution (e.g., Day-Lewis et al. 2005; Singha and Moysey 2006; Singha et al. 2007). Therefore, scanning a training image horizontally, that is, moving through a single 2-D image until a certain data event is scanned, can produce large bias since it treats the tomograms as if resolution is constant in space. To overcome this, we stacked a large number of realizations of a training image and the corresponding tomograms, similar to Zhou et al. (2012).

Technically speaking, a 3-D training image with four variables is set up. In our case, this constitutes two stacks of the catalogue of the categorical training images and

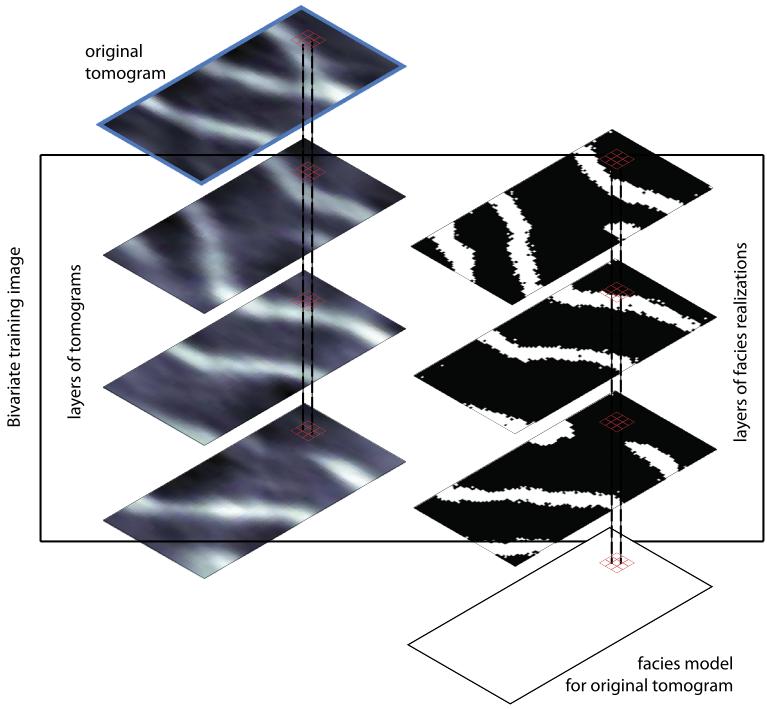

Fig. 2 The sampling principle used to account for the spatially variable resolution of geophysical tomograms

the corresponding tomograms. The other two variables are the x- and y-coordinates of all nodes. By doing so, we treat the individual layers of the stacks as projections of a single plane and sample for 2-D patterns within these bodies. The x- and y-coordinates are dummy variables needed to keep the MPDS algorithm from seeking data events in 3-D. The 'working TI' is thus scanned until a data event is found for which

- the distance between the pattern in the *facies* variable and the pattern formed by the already simulated pixels in the simulations grid is below the threshold t_{facies},
- the distance between the pattern in the *tomogram* variable and the pattern in the conditioning tomogram is below the threshold t_{tomogram} and
- the distances between the x- and y-coordinates of the pixel of interest and the undefined pixel in the data event are below thresholds t_x and t_y.

Once this data event is found in the *tomogram* variable of the 'working TI', the value for the pixel of interest is pasted from the *facies* variable in the 'working TI' and copied to the simulation grid. Figure 2 depicts the general scanning procedure. The possibility to deal with multiple variables, whether categorical or continuous, is an advantage of MPDS over conventional MPS algorithms.

2.4 Forward Modeling

Though the framework of our approach is general in terms of the type of tomograms used, we will now focus on applications to cross-hole GPR tomograms. In cross-hole GPR experiments, transmitter and receiver antennas are placed in adjacent boreholes and the subsurface electromagnetic properties are sensed by measuring the transmitted signal for different transmitter-receiver configurations. Here, we focus on the first arrivals of the radar wave, which bear information about the radar wavespeed in the interwell region. In our first application, we assume that the relation between the facies type and the radar wavespeed is known (in practice, this could be known from laboratory experiments). In our second application, detailed information about the porosity and the hydraulic conductivity of each facies type are available. The porosity information for the individual facies was translated into values of radar wavespeed v using (Sen et al. 1981)

$$\epsilon = \epsilon_w \phi^m \left(\frac{1 - \frac{\epsilon_m}{\epsilon_w}}{1 - \frac{\epsilon_m}{\epsilon}} \right)^m \tag{3}$$

and (e.g., Davis and Annan 1989)

$$v = \frac{c}{\sqrt{\epsilon}}, \tag{4}$$

where ϵ_w, ϵ_m and ϵ [-] are the relative electrical permittivity of water, of the grains and of the bulk material, respectively. We here used $\epsilon_w = 81$ and $\epsilon_m = 3$. The porosity of each facies is ϕ, the so-called cementation factor m is typically taken to be 1.5 in unconsolidated media and the speed of light $c = 3 \times 10^8$ m/s.

Based on the velocity model, we determined radar traveltimes for a cross-hole GPR experiment using

$$t_{\mathrm{GPR}} = \int_{\mathbf{x}_1}^{\mathbf{x}_2} u(s)\, ds, \tag{5}$$

where $u(s)$ [s/m] is the radar slowness (i.e., the reciprocal of the radar wavespeed) along the trajectory s, starting at point $\mathbf{x}_1$ and ending at $\mathbf{x}_2$. The trajectories of the radar signals are dependent on the spatial distribution of the radar wavespeed. We solve the eikonal equation to get the spatial distribution of first-arrival traveltimes for each source location using the finite-difference algorithm of Podvin and Lecomte (1991) and perform ray-tracing by back-propagation for each receiver location (Vidale 1988).

In the two applications considered below, transmitters and receivers were placed at the left and right boundary of the model domain at a spacing of 0.25 m and experiments were repeated for reciprocal transmitter and receiver boreholes so that transmitter positions become receiver positions and vice versa. As is common practice, only rays for which the transmitter-receiver path is inclined less than 50° to the horizon are taken into account (e.g., Peterson 2001). This resulted in data sets of 2430 and 1388 traveltimes for the first and second application. All synthetic radar data were contaminated with Gaussian noise corresponding to a relative error of 1 % of the measurement value.

Table 1 Overview of MPDS parameters. The summation signs denote that the simple sum of non-matching nodes is taken as a distance measure. The scan fraction f is a parameter for the multivariate TI and is not chosen for each individual variables

Variable	n	t	f	n-density	Distance type
Case 1: Channels					
facies	25	0.04	0.1	1.0	$\sum$
tomogram	25	0.04	0.1	1.0	ℓ_1-norm
x-coordinate	1	0.06	0.1	1.0	ℓ_1-norm
y-coordinate	1	0.03	0.1	1.0	ℓ_1-norm
Case 2: Herten					
facies	25	0.04	0.1	0.5	$\sum$
tomogram	25	0.04	0.1	0.5	ℓ_1-norm
x-coordinate	1	0.03	0.1	1.0	ℓ_1-norm
y-coordinate	1	0.02	0.1	1.0	ℓ_1-norm

3 Application to a Channel Scenario

We first applied the method to a two-facies case featuring channel-like structures (Strebelle 2002). Radar wavespeeds of 70 and 80 m/μs were assigned to facies 0 and 1, respectively. A total of 1000 realizations of the original TI (generated with *DeeSse*, with a resolution of 0.1×0.1 m) and the corresponding tomograms build the bivariate working TI from which we sample. The number of neighboring nodes n in the simulation defines the order of the statistics that are honored during the simulation. For the facies variable, the number of neighboring nodes is set to $n = 25$ and the distance threshold to $t_{\text{facies}} = 0.04$. This means that if no more than one of the 25 nearest cells ($25 \times 0.04 = 1$) around the cell to be simulated differs from the cell values in the data event, the pattern for this variable is considered acceptable (Mariethoz et al. 2010a). For the tomogram variable, the same parameters are used ($n = 25$ and $t_{\text{tomogram}} = 0.04$), whereas for the dummy variables (i.e., the x- and y-coordinates), we choose $n = 1$ and the distance thresholds t_x and t_y so that the data events used for simulation are in an area that differs maximally three grid cells in x- and y-direction from the simulation cell (Table 1).

Results are shown in Fig. 3. The tomograms clearly highlight the smearing effect inherent in smoothness-constrained tomography: Even if the true image is built up only by two facies (black and white), classical tomography always produces shades of gray. A total of 100 MPDS simulations, conditioned to the original tomogram, were generated with *DeeSse*. For each simulation, we calculated the radar traveltimes and compared them to the true radar data. Keeping only simulations for which the WRMSE is below 1.0, left us with 68 simulations (Fig. 4a). For illustration of the MPDS simulations with different conditioning (Fig. 5), we adapted the so-called movie strategy for the visualization of stochastic inversion results (Tarantola 2005). As expected, the conditioning to a tomogram brings the simulations closer to the true facies model. For simulated facies models that fail to predict the true radar traveltimes, the main structures of the true model are reproduced, but they often fail to represent the connectivity of the channels. The accepted facies models are visually very similar to the true facies model and the connectivity of the channels is recovered.

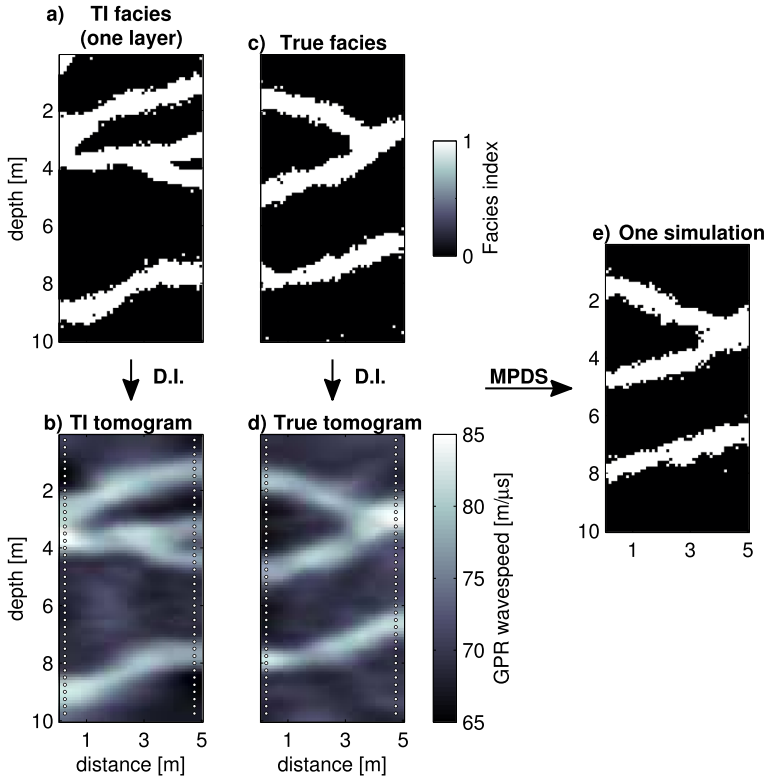

Fig. 3 (**a**) and (**b**): One layer of the bivariate training image; (**a**) facies and (**b**) corresponding tomogram. (**c**) The true facies we seek to recover and (**d**) its tomogram, which is used as conditioning data in the MPDS simulations. D.I. stands for deterministic inversion. *White dots* indicate transmitter and receiver positions for the radar traveltime calculations. (**e**) One simulated facies model

4 Application to a Multi-facies Aquifer Analog

As a more realistic example, we applied our methodology to a facies model based on a detailed gravel aquifer mapping study (Bayer et al. 2011). The underlying model includes features that are typical for aquifers built up by alluvial gravel deposits. These types of aquifer bodies are of high importance in many parts of the world due to their generally high storage capacity, high permeability and accessibility.

4.1 The Herten Aquifer Analog

The Herten aquifer model is based on detailed mapping of sedimentary deposits in a gravel pit in southwest Germany. Bayer et al. (2011) set up a geological map of the deposits to establish a realistic aquifer analog. The analog is a 3-D representation of the gravel body, which was made possible by mapping during ongoing excavation. The deposits are mainly formed by unconsolidated fluvio-glacial and fluvial sediments in the Rhine basin (Bayer et al. 2011). The dominant structural elements, erosional surfaces, scours, gravel sheets, are typical for sediments deposited in braided river

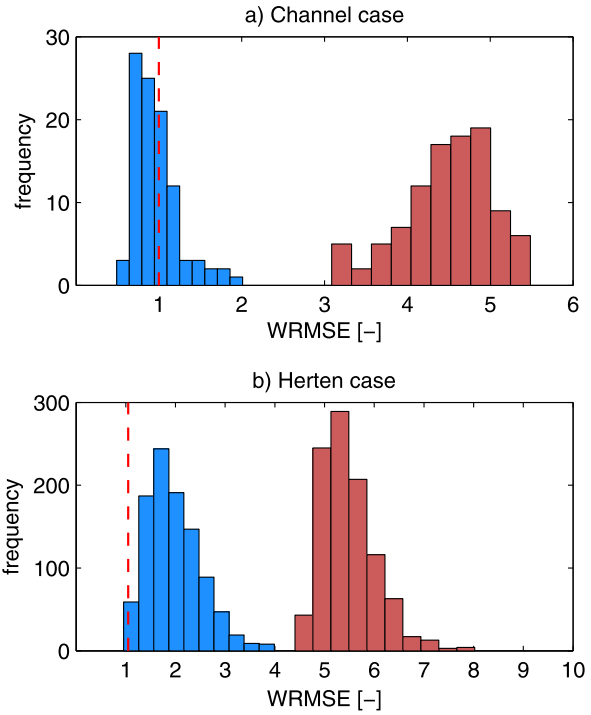

Fig. 4 (**a**) Distribution of weighted root-mean squared errors (WRMSE) of radar traveltimes for 100 unconditioned (*red*) and conditioned (*blue*) MPDS simulations for the channel scenario. The acceptance threshold (*dashed vertical line*) is the same as for the deterministic inversion. 68 % of the conditioned simulations predict traveltimes with an WRMSE below the indicated threshold of 1.0 (*red line*). (**b**) As for a, but for the Herten case and for 1000 unconditioned and conditioned simulations. Ten conditioned simulations predict the traveltimes with an WRMSE below the threshold of 1.05

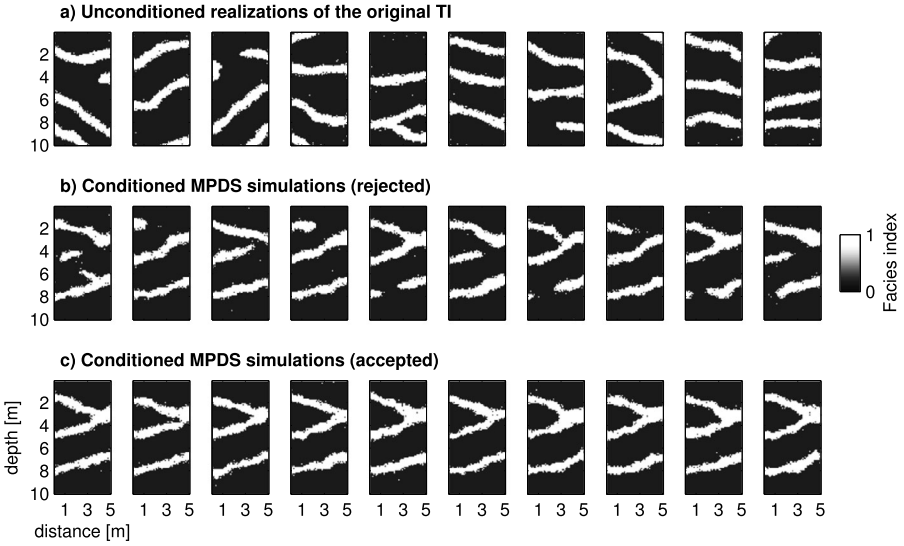

Fig. 5 Different MPDS simulations of the channel scenario in movie illustration. (**a**) Unconditioned simulations as they are used as layers of the 'working training image'. (**b**) MPDS simulations conditioned to a geophysical tomogram. These simulations failed to predict the radar data satisfactorily and were rejected. (**c**) As for (**b**) but with radar traveltimes for which the WRMSE is below the threshold, these simulation were accepted

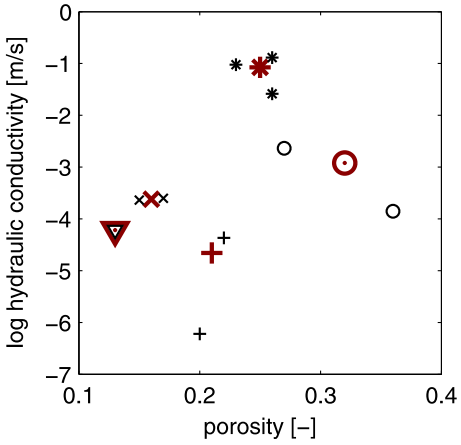

Fig. 6 Clustering of the original 10 facies to the reduced facies distribution. *Vertical crosses* (denoted facies 1 in Table 2), *circles* (facies 2), *triangles* (facies 3), *diagonal crosses* (facies 4) and *asterisks* (facies 5) refer to the simplified facies model. In *red* the new facies

Table 2 Description of the different facies types

Facies index	Description	Hydraulic conductivity K [m/s]	Porosity [-]
1 (+)	Alternating gravel, bimodal basal subunit (sand, silt, clay)	2.2×10^{-5}	0.21
2 (∘)	Well-sorted gravel and sand	1.2×10^{-3}	0.32
3 (▽)	Sand-rich, poorly sorted, matrix supported gravel	6.1×10^{-5}	0.13
4 (×)	Poorly sorted, matrix supported gravel	2.4×10^{-4}	0.16
5 (∗)	Alternating gravel, open framework	8.4×10^{-2}	0.25

environments. Ten different subunitary lithofacies are defined to describe the gravel deposits. For every lithofacies, porosity and hydraulic conductivity values and ranges are provided by experimental studies of Bayer (2000), Heinz et al. (2003) and Kostic et al. (2005).

The detailed aquifer analog was digitized to use it as a base for geostatistical simulations (Comunian et al. 2011). We used a 2-D slice of the Herten analog as a conceptual model, that is, as an original training image. The dimensions of one slice of the analog are 7×16 m. We generated 1000 realizations of the original training image with *DeeSse*. All realizations show some of the geological patterns and of the lithofacies found in the analog, but the direction and dimension of these patterns varies between the realizations. The ensemble of realizations consequently represents a rather wide variety of geological scenarios.

For this study, the available facies realizations were simplified in that (1) only a 7×4 m part of the images were considered for simulation (keeping the original cell size of 0.05×0.05 m) and (2) the number of facies was reduced from 10 to 5 by clustering similar facies together. The clustering is based on both similarities in geological texture (Bayer et al. 2011), as well as in hydrogeological properties (Fig. 6). The modified facies and their properties are summarized in Table 2.

4.2 Results

We chose slightly different parameters in the MPDS algorithm to account for the higher degree of complexity in this multi-facies case. To define a data event for the facies and radar wavespeed ('tomogram') parameters, the maximum density of neighboring nodes within the search environment was reduced to 0.5 to capture more complex patterns and to prevent just reproducing overly fine small-scale variations. This means that we consider n out of the $2n$ closest cells for pattern definition. Again, the distance thresholds for the x- and y-coordinates, t_x and t_y, were chosen such that the node to be simulated is constrained solely by data events occurring in the same region of the grid (Table 1).

Unlike the tomograms, the simulations feature the desired sharp interfaces between facies (Fig. 7). Typical facies-in-facies patterns (e.g., facies 1 and 5 are frequently connected in tight layering) are reproduced rather well. We simulated 1000 facies models, of which 10 predicted the radar traveltimes within the error bounds (Fig. 4b). Different simulations that predict the radar data within the error bounds are displayed in Fig. 8.

We face two different problems when simulating facies models based on the Herten TI. (1) The complexity of the realizations leads to higher computational costs since it takes a longer time until a suitable data event is found in the TI. Also, the choice of the simulation parameters becomes more crucial than in the simpler channel case. (2) Many conditioned simulations feature small-scale structures that are not present in the true facies model. Together with the wide range of radar wavespeeds (much larger than for the channel scenario), this leads to a high number of conditioned simulations that fail to predict the radar data within the defined error bounds. Thus, more simulations are required to get a decent number of conditioned simulations that honor the geophysical data and not only patterns in the tomograms.

5 Impact on Flow Predictions

The main purpose for determining the spatial distribution of lithofacies and their hydrological parameters with high resolution is to use these models for prediction of flow or solute transport. To demonstrate the improvement of the models resulting from bivariate simulation, we conducted synthetic tracer experiments and compared unconditioned (i.e., the layers of the facies training image) and conditioned MPDS simulations with respect to their transport predictions. Tracer breakthrough at certain locations on the right boundary is calculated for an injection of a conservative tracer at the left boundary of the domain that is driven by a horizontal head gradient. We used the finite-difference code MaFloT (Matlab Flow and Transport (maflot.com), Künze and Lunati 2012) to solve the advection-dispersion equation and calculate the tracer concentration evolution during continuous tracer injection. For dispersivities in longitudinal and transversal direction, we used $\alpha_l = 10^{-2}$ m and $\alpha_t = 10^{-3}$ m and for molecular diffusion $D = 10^{-9}$ m^2/s.

For the channel scenario, hydraulic conductivity values of $K_0 = 10^{-5}$ m/s and $K_1 = 10^{-2}$ m/s were assigned to facies 0 and 1, respectively, to model highly con-

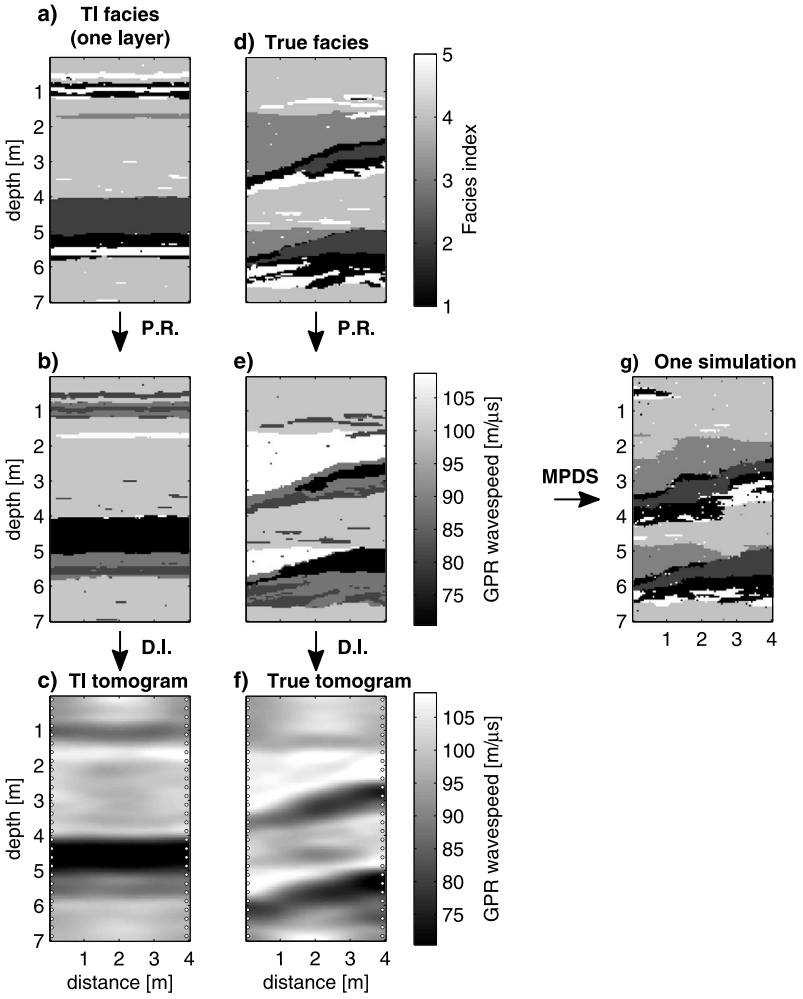

Fig. 7 (**a**) One layer of the facies training image and (**b**) corresponding radar wavespeed distribution, obtained by applying a petrophysical relation (P.R.). (**c**) The corresponding tomogram results from deterministic inversion (D.I.) of (**b**). (**d**) The true facies we seek to recover, (**e**) its wavespeed distribution and (**f**) its tomogram, which is used as conditional data in the MPDS simulations. *White dots* indicate transmitter and receiver positions for the radar traveltime calculations. (**g**) One simulated facies model

ductive channels in a low-conductivity matrix. The porosity was kept constant at $\phi = 0.3$. For the aquifer analog (Herten), hydrogeological facies information, that is, the porosity and the hydraulic conductivity values were directly available from an outcrop data set (Table 2).

In both cases, the uncertainty in the predictions for the tracer breakthrough is clearly reduced for the simulations that are conditioned to a tomogram (Fig. 9). For simulations that predict the radar traveltimes within the error bounds, the uncertainty is further reduced. There is no indication of modeling bias, the predicted breakthroughs are consistent with the breakthrough curves of the true models.

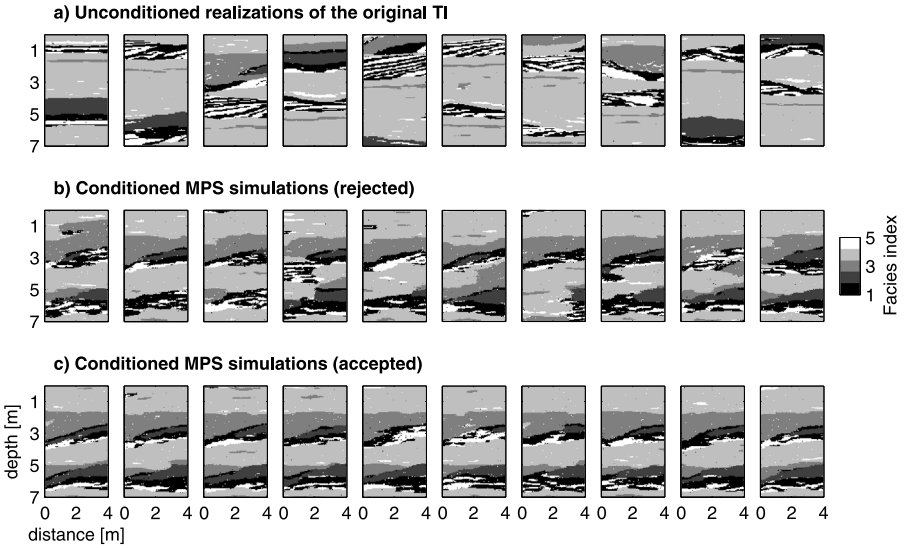

Fig. 8 Different MPDS simulations of the Herten training image in movie illustration. (**a**) Unconditioned simulations as they are used as layers of the training image. (**b**) MPDS simulations conditioned to a geophysical tomogram. These simulations failed to predict the radar data satisfactorily and were rejected. (**c**) As for (**b**) but with radar traveltimes for which the WRMSE is below the threshold, these simulation were accepted

6 Discussion

We show that combining MPS simulations and classical geophysical tomography can produce models that overcome some of the shortcomings of both purely tomogram-based inverse models and unconditioned MPS simulations. Unlike classical geophysical tomography, the presented method allows to recover models that feature expected geological patterns and sharp interfaces between facies elements. At the same time, the inverse models are constrained by geophysical data whose information is spread over large parts of the model domain, which is not the case for unconditioned simulations or simulations conditioned to point data only. When applied in practice, the following issues must be taken into account:

- As for all methods that include MPS simulations, the choice of an adequate training image is of utmost importance. If no auxiliary geological information is available, MPS simulations carry a substantial risk of creating illusive results. This was observed in tests performed by applying the method with a poorly chosen TI: We tried to represent an object-based model featuring lenses with the same channel TI as used in the first application. The resulting models reproduce the overall distribution of the two facies but feature channels instead of lenses and fail to predict the data well. Problems in finding models with satisfactory data fit can thus be taken as an indicator for an incomplete or biased TI. A detailed assessment about how a poorly chosen TI affects the quality of MPS simulations is beyond the scope of this study and is left as a recommendation for further research.

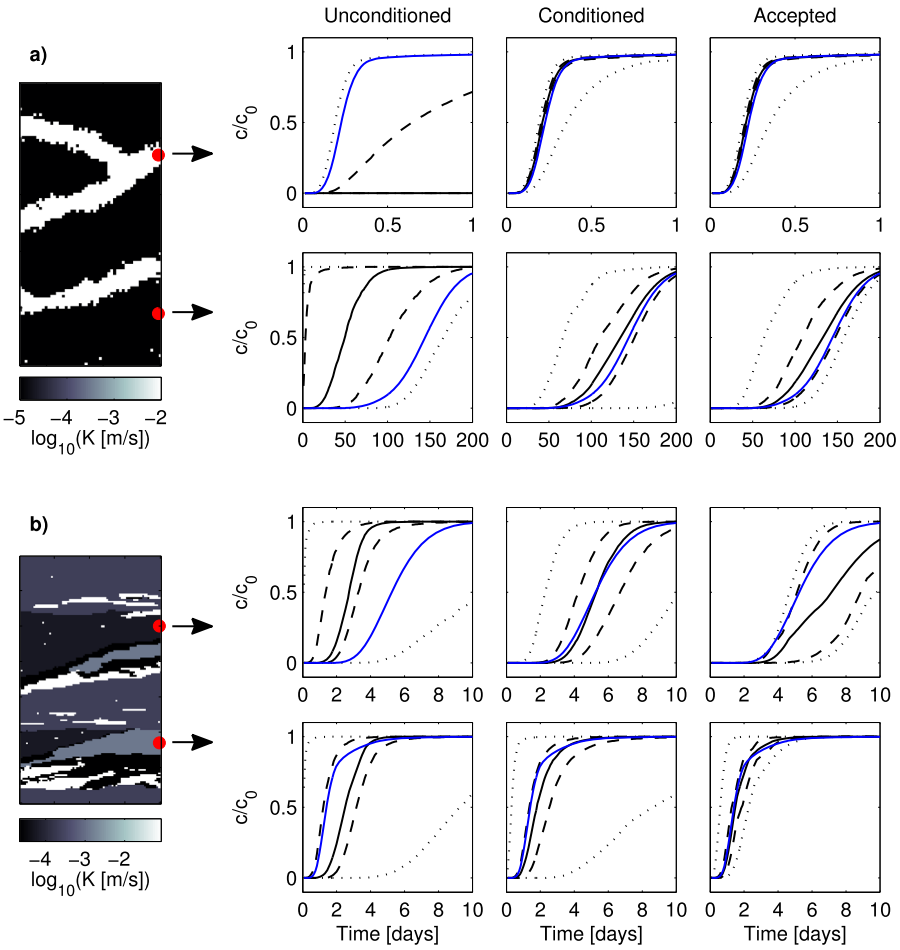

Fig. 9 Statistics of calculated breakthrough curves for (**a**) channel scenario and (**b**) Herten scenario. *Solid*, *dashed* and *dotted lines* depict mean, 50 % quantiles and 95 % quantiles. *Blue line*: breakthrough of the true model

- In the current formulation, the GPR signals are approximated by curved rays rather than accounting for the full-waveform signal. This approximation has been proven robust in many applications (e.g., Davis and Annan 1989; Alumbaugh et al. 2002; Dafflon and Barrash 2012). New developments in full-waveform inversion techniques (e.g., Meles et al. 2011; Klotzsche et al. 2012) promise improved inversion results for certain settings if further attributes of the waveform than just the first arrival are considered.
- In the two scenarios presented, we assumed the petrophysics (i.e., the relationship between the lithological properties and the geophysical parameters) to be perfectly known and exact, which is rarely the case in practice. We postulate that the uncertainty of the petrophysics can be accounted for by using a much larger TI that

contains several tomograms for one facies model, each calculated with different petrophysical parameters. We leave this for further research.
- We applied the method to cross-hole GPR tomograms, but the method is general with regard to the measured geophysical signal. Applications to other geophysical or hydrological tomographic methods, such as electrical resistivity tomography (ERT), seismic tomography or hydraulic tomography are straightforward.

The 'weight' of the facies TI versus the conditioning data can be changed by varying the MPDS parameters. For a smaller distance threshold t, for example, patterns in the TI are reproduced more accurately. This requires larger parts of the TI to be scanned in order to find a matching data event. Thus in general, the choice of the sampling parameters is a compromise between reproduction accuracy and computational effort and to a large part controls the CPU burden in our workflow (Meerschman et al. 2013). Another computationally expensive step is creating the working TI, since each generation of a MPDS realization of the original TI is followed by a forward calculation and a geophysical inversion. However, the inversion parameters are taken as in the inversion of the field data, which implies that constructing the working TI demands no extensive parameter study and needs to be done only once.

Like purely stochastic inversions based on Markov chain Monte Carlo, the proposed method provides the user with an ensemble of possible models (e.g., Cordua et al. 2012). Since the models are not extracted from a Markov chain and are intrinsically uncorrelated, our method is significantly faster than stochastic inversions. Applying the method to a 3D case is straightforward, but CPU restrictions are non-negligible.

The quality of a geophysical inverse model strongly depends on the choice of the inversion parameters. This problem is largely circumvented by our approach, since we do not use the tomogram for interpretation but for conditioning of a geological conceptual model. We implicitly account for the resolution limitations of tomograms, thus there is no need for an explicit resolution analysis. Also, we create several possible models, which are used to assess the uncertainty in the modeling results. This highlights the improvement over interpretation of individual tomograms, where accurate estimation of both resolution and uncertainty generally remains difficult (e.g., Williamson 1991; Day-Lewis and Lane 2004; Doser et al. 1998).

The resulting models reproduce the large- and small-scale structures of the true models rather well. They can be used for geological interpretation or as starting points for further inversion or conditioning. Additional reduction of the uncertainty in the parameter estimations might be achieved by including other types of geophysical or hydrological data in the presented workflow.

7 Conclusions

A method is presented to condition MPS simulations to geophysical tomograms. We create facies simulations by scanning a bivariate training image, constructed from geological facies realizations and their tomograms, for patterns found in a conditioning

tomogram. This allows to exploit the advantages of both tomography and multiple-point geostatistical simulation. MPS simulations produce detailed facies models with sharp interfaces, where realistic geological constraints are honored by sampling from a TI. Conditioning the simulations to a tomogram that resolves large-scale features over large parts of the model domain, allows to adequately recover realistic facies models. We found running a geophysical forward calculation on the proposed simulations and comparing the response to the measured data to be a valid acceptance criterion. Unlike the classical geophysical approach where the interpreter is left with one tomographic image, the method provides an ensemble of possible facies models that allows for uncertainty assessment. Testing the conditioned simulations with respect to their transport predictions reveals that they correctly predict the transport characteristics of the true model and that the uncertainty is reduced compared to predictions of unconditioned MPS simulations.

Acknowledgements This research was funded by the Swiss National Science Foundation (SNF) and is a contribution to the ENSEMBLE project (grant no. CRSI22_132249). We would like to thank Philippe Renard for many helpful suggestions during the course of this study. We thank the three anonymous reviewers for their constructive comments that helped to improve the manuscript.

References

Alharthi A, Lange J (1987) Soil water saturation: dielectric determination. Water Resour Res 23(4):591–595

Alumbaugh D, Chang P, Paprocki L, Brainard J, Glass R, Rautman C (2002) Estimating moisture contents in the vadose zone using cross-borehole ground penetrating radar: a study of accuracy and repeatability. Water Resour Res 38(12):1309

Bayer P (2000) Aquifer-Analog-Studie in grobklastischen 'braided river' Ablagerungen: Sedimentäre/hydrogeologische Wandkartierung und Kalibrierung von Georadarmessungen—Diplomkartierung. Master's thesis, University of Tübingen, Tübingen, Germany (in German)

Bayer P, Huggenberger P, Renard P, Comunian A (2011) Three-dimensional high resolution fluvio-glacial aquifer analog: part 1: Field study. J Hydrol 405:1–9

Caers J, Ma X (2002) Modeling conditional distributions of facies from seismic using neural nets. Math Geol 34(2):143–167

Cardiff M, Kitanidis P (2009) Bayesian inversion for facies detection: an extensible level set framework. Water Resour Res 45(10):W10416

Coléou T, Poupon M, Azbel K (2003) Unsupervised seismic facies classification. Lead Edge 22(10):942–953

Comunian A, Renard P, Straubhaar J, Bayer P (2011) Three-dimensional high resolution fluvio-glacial aquifer analog: part 2: Geostatistical modeling. J Hydrol 405:10–23

Constable S, Parker R, Constable C (1987) Occam's inversion: a practical algorithm for generating smooth models from electromagnetic sounding data. Geophysics 52(3):289–300

Cordua K, Hansen T, Mosegaard K (2012) Monte Carlo full-waveform inversion of crosshole GPR data using multiple-point geostatistical a priori information. Geophysics 77(2):H19–H31

Dafflon B, Barrash W (2012) Three-dimensional stochastic estimation of porosity distribution: benefits of using ground-penetrating radar velocity tomograms in simulated-annealing-based or Bayesian sequential simulation approaches. Water Resour Res 48(5):W05553

Davis J, Annan A (1989) Ground-penetrating radar for high-resolution mapping of soil and rock stratigraphy. Geophys Prospect 37(5):531–551

Day-Lewis F, Lane J Jr (2004) Assessing the resolution-dependent utility of tomograms for geostatistics. Geophys Res Lett 31(7):L07503

Day-Lewis F, Singha K, Binley A (2005) Applying petrophysical models to radar travel time and electrical resistivity tomograms: resolution-dependent limitations. J Geophys Res 110(B8):B08206

de Matos M, Osorio P, Johann P (2007) Unsupervised seismic facies analysis using wavelet transform and self-organizing maps. Geophysics 72(1):P9–P21
Doser D, Crain K, Baker M, Kreinovich V, Gerstenberger M (1998) Estimating uncertainties for geophysical tomography. Reliab Comput 4(3):241–268
Eppstein M, Dougherty D (1998) Efficient three-dimensional data inversion: soil characterization and moisture monitoring from cross-well ground-penetrating radar at a Vermont test site. Water Resour Res 34(8):1889–1900
Gómez-Hernández J, Wen X (1998) To be or not to be multi-Gaussian? A reflection on stochastic hydrogeology. Adv Water Resour 21(1):47–61
Heinz J, Kleineidam S, Teutsch G, Aigner T (2003) Heterogeneity patterns of quaternary glaciofluvial gravel bodies (SW-Germany): application to hydrogeology. Sediment Geol 158(1–2):1–23
Hu L, Chugunova T (2008) Multiple-point geostatistics for modeling subsurface heterogeneity: a comprehensive review. Water Resour Res 44(11):W11413
Hubbard S, Chen J, Peterson J, Majer E, Williams K, Swift D, Mailloux B, Rubin Y (2001) Hydrogeological characterization of the South Oyster Bacterial Transport Site using geophysical data. Water Resour Res 37(10):2431–2456
Hubbard S, Rubin Y (2000) Hydrogeological parameter estimation using geophysical data: a review of selected techniques. J Contam Hydrol 45(1–2):3–34
Journel A, Posa D (1990) Characteristic behavior and order relations for indicator variograms. Math Geol 22(8):1011–1025
Kitanidis P (1997) Introduction to geostatistics: applications in hydrogeology. Cambridge University Press, Cambridge
Klotzsche A, van der Kruk J, Meles G, Vereecken H (2012) Crosshole gpr full-waveform inversion of waveguides acting as preferential flow paths within aquifer systems. Geophysics 77(4):H57–H62
Kostic B, Becht A, Aigner T (2005) 3-D sedimentary architecture of a quaternary gravel delta (SW-Germany): implications for hydrostratigraphy. Sediment Geol 181(3):147–171
Krishnan S, Journel A (2003) Spatial connectivity: from variograms to multiple-point measures. Math Geol 35(8):915–925
Künze R, Lunati I (2012) An adaptive multiscale method for density-driven instabilities. J Comput Phys 231:5557–5570
Linde N, Binley A, Tryggvason A, Pedersen L, Revil A (2006) Improved hydrogeophysical characterization using joint inversion of cross-hole electrical resistance and ground-penetrating radar traveltime data. Water Resour Res 42(12):W04410
Mariethoz G, Renard P, Caers J (2010a) Bayesian inverse problem and optimization with iterative spatial resampling. Water Resour Res 46(11):W11530
Mariethoz G, Renard P, Straubhaar J (2010b) The direct sampling method to perform multiple-point geostatistical simulations. Water Resour Res 46(11):W11536
Meerschman E, Pirot G, Mariethoz G, Straubhaar J, Meirvenne M, Renard P (2013) A practical guide to performing multiple-point statistical simulations with the direct sampling algorithm. Comput Geosci 52:307–324
Meles G, Greenhalgh S, der Kruk J, Green A, Maurer H (2011) Taming the non-linearity problem in GPR full-waveform inversion for high contrast media. J Appl Geophys 73:174–186
Menke W (1989) Geophysical data analysis: discrete inverse theory, vol 45. Academic Press, New York
Moysey S, Caers J, Knight R, Allen-King R (2003) Stochastic estimation of facies using ground penetrating radar data. Stoch Environ Res Risk Assess 17(5):306–318
Moysey S, Knight R, Jol H (2006) Texture-based classification of ground-penetrating radar images. Geophysics 71(6):K111–K118
Moysey S, Singha K, Knight R (2005) A framework for inferring field-scale rock physics relationships through numerical simulation. Geophys Res Lett 32:L08304
Ory J, Pratt R (1995) Are our parameter estimators biased? The significance of finite-difference regularization operators. Inverse Probl 11:397–424
Paige C, Saunders M (1982) LSQR: an algorithm for sparse linear equations and sparse least squares. ACM Trans Math Softw 8(1):43–71
Peterson J (2001) Pre-inversion corrections and analysis of radar tomographic data. J Environ Eng Geophys 6:1–18
Podvin P, Lecomte I (1991) Finite difference computation of traveltimes in very contrasted velocity models: a massively parallel approach and its associated tools. Geophys J Int 105(1):271–284
Rankey E, Mitchell J (2003) That's why it's called interpretation: impact of horizon uncertainty on seismic attribute analysis. Lead Edge 22(9):820–828

Rauber M, Stauffer F, Huggenberger P, Dracos T (1998) A numerical three-dimensional conditioned/unconditioned stochastic facies type model applied to a remediation well system. Water Resour Res 34(9):2225–2233

Richardson J, Sangree J, Sneider R (1987) Applications of geophysics to geologic models and to reservoir description. J Pet Technol 39(7):753–755

Roth K, Schulin R, Flühler H, Attinger W (1990) Calibration of time domain reflectometry for water content measurement using a composite dielectric approach. Water Resour Res 26(10):2267–2273

Sen P, Scala C, Cohen M (1981) A self-similar model for sedimentary rocks with application to the dielectric constant of fused glass beads. Geophysics 46(5):781–795

Singha K, Day-Lewis F, Moysey S (2007) Accounting for tomographic resolution in estimating hydrologic properties from geophysical data. In: Hyndman DW, Day-Lewis FD, Singha K (eds) Subsurface hydrology: data integration for properties and processes. Geophysical monograph series, vol 171. AGU, Washington, pp 227–242

Singha K, Moysey S (2006) Accounting for spatially variable resolution in electrical resistivity tomography through field-scale rock-physics relations. Geophysics 71(4):A25

Straubhaar J, Renard P, Mariethoz G, Froidevaux R, Besson O (2011) An improved parallel multiple-point algorithm using a list approach. Math Geosci 43:305–328

Straubhaar J, Walgenwitz A, Renard P (2013) Parallel multiple-point statistics algorithm based on list and tree structures. Math Geosci 45(2):1–17

Strebelle S (2002) Conditional simulation of complex geological structures using multiple-point statistics. Math Geol 34(1):1–21

Tarantola A (2005) Inverse problem theory and methods for model parameter estimation. Society for Industrial Mathematics

Tinga W, Voss W, Blossey D (1973) Generalized approach to multiphase dielectric mixture theory. J Appl Phys 44(9):3897–3902

Tran T (1994) Improving variogram reproduction on dense simulation grids. Comput Geosci 20(7):1161–1168

Vidale J (1988) Finite-difference calculation of travel times. Bull Seismol Soc Am 78(6):2062–2076

Western A, Blöschl G, Grayson R (2001) Toward capturing hydrologically significant connectivity in spatial patterns. Water Resour Res 37(1):83–97

Williamson P (1991) A guide to the limits of resolution imposed by scattering in ray tomography. Geophysics 56(2):202–207

Zhou H, Gómez-Hernández J, Li L (2012) A pattern-search-based inverse method. Water Resour Res 48(3):W03505

Zinn B, Harvey C (2003) When good statistical models of aquifer heterogeneity go bad: a comparison of flow, dispersion, and mass transfer in connected and multivariate Gaussian hydraulic conductivity fields. Water Resour Res 39(3):1051